energies

MDPI

Article

Seismic Anisotropic Fluid Identification in Fractured Carbonate Reservoirs

Xiaolong Guo [1], Bin Yan [2,*], Juyi Zeng [3], Guangzhi Zhang [2,*], Lin Li [2], You Zhou [2] and Rui Yang [2]

[1] Research Institute of Petroleum Exploration and Development, PetroChina, Beijing 100083, China
[2] School of Geosciences, China University of Petroleum (East China), Qingdao 266580, China
[3] Guizhou Energy Industry Research Institute Co., Ltd., Guiyang 550000, China
* Correspondence: s20010098@s.upc.edu.cn (B.Y.); zhanggz@upc.edu.cn (G.Z.)

Abstract: Seismic fluid identification plays an important role in reservoir exploration and development. Natural vertical fractures are common in carbonate rocks, it is essential to consider fracture-induced anisotropy in the fluid identification of fractured carbonate reservoirs. We have developed a novel Bayesian elastic impedance variation with an angle and azimuth (EIVAZ) inversion approach for directly estimating the fracture fluid indicator (*FFI*), which can avoid cumulative errors produced in the indirect calculation process. Under the assumption of weak anisotropy and a small incident angle, we first derive a new approximate PP-wave coefficient for horizontal transverse isotropic (HTI) media. Analysis shows that the new approximation has reasonable accuracy at angles of incidence less than 30°. To estimate the *FFI* from observed azimuthal P-wave seismic reflection data, we further deduce the azimuthal *EI* equation and establish a two-step inversion workflow. Finally, the proposed approach is demonstrated by tests on a synthetic data example and a field data set of a fractured carbonate reservoir in the Sichuan Basin (China). Results show that the model parameters can be reasonably estimated even with moderate noise levels. The estimated *FFI* and quasi-normal fracture weakness show relatively high values at the location of reservoirs, which reliably indicate a fractured gas-bearing reservoir.

Keywords: fluid identification; fracture detection; fractured carbonate reservoirs; elastic impedance variation with angle and azimuth (EIVAZ)

Citation: Guo, X.; Yan, B.; Zeng, J.; Zhang, G.; Li, L.; Zhou, Y.; Yang, R. Seismic Anisotropic Fluid Identification in Fractured Carbonate Reservoirs. *Energies* **2022**, *15*, 7184. https://doi.org/10.3390/en15197184

Academic Editor: Ingo Pecher

Received: 8 July 2022
Accepted: 21 September 2022
Published: 29 September 2022

1. Introduction

Reservoir fluid identification is an important part of oil and gas reservoir exploration and reservoir evaluation [1–4]. Ostrander [1] used the amplitude variation with offset (AVO) bright spot technique to solve the problem of fluid identification in gas-bearing sandstone reservoirs. Rutherford [2] and Castagna et al. [3] classified AVO types according to AVO response characteristics, which laid the foundation for AVO analysis techniques. The AVO analysis technique is a qualitative analysis of reservoir fluid characteristics but with certain limitations. With the development of petrophysics and the advancement of seismic inversion technology, the fluid identification method based on reservoir elasticity has become the mainstream technology for reservoir hydrocarbon identification at this stage. Smith and Gidlow [5] showed that the weighted superposition of relative changes in P- and S-wave velocities can be used to discern hydrocarbon-bearing anomalies in reservoirs. Using this method of weight difference operation, many scholars have proposed different effective fluid indicators. Goodway et al. [6] proposed the reservoir fluid identification technique using the Lamé parameter. Gray [7] pointed out that the Lamé parameter could be directly regarded as a fluid indicator for reservoir fluid. Based on both Biot and Gassmann's theories for fluid-saturated porous rocks, a general formula is derived for fluid-indicator discrimination given that both the P- and S-impedances are available [8]. Russell et al. [9] derived the AVO approximation formula containing the Gassmann fluid

term and achieved the direct inversion of the Gassmann fluid term. Compared with the Gassmann fluid term, the fluid bulk modulus is more effective in distinguishing reservoir fluid types when the degree of reservoir rock consolidation is low, or the porosity varies significantly [10]. Yin et al. [11] chose the fluid bulk modulus as a fluid indicator to improve the sensitivity of fluid indication. However, these fluid indicators fail to consider the effect of anisotropy caused by fractures in the reservoir and are less applicable in fractured carbonate reservoirs.

Numerous experiments have shown that most crustal rocks are anisotropic. Natural vertical fractures are common in carbonate rocks. A fractured carbonate reservoir can be equivalent to a horizontal transverse isotropic (HTI) medium with a set of vertically oriented fractures [12,13]. The presence of aligned vertical fractures makes the media azimuthally anisotropic and can cause the reflection amplitudes or velocities of seismic waves to vary with azimuth [14]. Therefore, it is essential to consider fracture-induced anisotropy in the fluid identification of fractured reservoirs. Schoenberg and Sayers [15] studied the effect of fracture fluids on the rock's physical parameters and utilized the ratio of normal to tangential compliance to identify fluid content filled in fractures. Pan et al. [16,17] discussed rock physics in the service of fluid identification and introduced the concept of quasi-fracture weaknesses and proposed a fracture fluid fracture indicator (*FFI*) parameterized by quasi-normal and tangential fracture weaknesses for fluid identification in fractured reservoirs. Chen et al. [18] proposed a modified fluid indicator (the ratio of Gassmann fluid term and porosity) that is more sensitive to fluid type and less affected by porosity. Golsanami et al. [19] discussed how the fluids in different types of reservoir pores and fractures could be identified by considering intergranular and intragranular pore space. P-wave azimuthal seismic reflection data have been widely used in fracture detection [20–23] and fluid identification [24–27]. For example, using the weak-anisotropy assumption [28], Chen et al. [24], Pan et al. [25], and Li et al. [27] developed amplitude variation with the angle and azimuth (AVAZ) inversion method to estimate fracture parameters (dry fracture weaknesses, dry compliances, and fracture density), fluid bulk modulus, or Gassmann fluid term for fracture detection and fluid identification. The elastic impedance (EI) was first proposed by Connolly [29] and then extended to anisotropic media by Martins [30]. Pan et al. [17,26] developed the elastic impedance variation with the angle and azimuth (EIVAZ) inversion method for fracture detection and fluid identification. The research results of many scholars show that the construction of a suitable anisotropic fluid indicator is necessary for the process of reservoir fluid identification. At the same time, appropriate inversion methods can lead to more accurate results.

Our objective is to realize seismic fluid identification in fractured carbonate reservoirs. We have developed a novel Bayesian EIVAZ inversion for the direct estimate of *FFI* proposed by Pan et al. [17], which can avoid cumulative errors produced in the indirect calculation process. Under the assumption of weak anisotropy and a small incident angle, we first derive a new approximate PP-wave coefficient as a function of P-wave impedance, P- to S-wave impedance ratio, *FFI*, and quasi-normal fracture weakness in an HTI medium and analyze the precision of the new approximation using a two-layer model. Next, we deduce the azimuthal EI equation and establish a two-step inversion workflow to estimate the *FFI* from observed azimuthal P-wave seismic reflection data. Finally, the proposed approach is demonstrated by tests on a synthetic data example and a field data set of a fractured carbonate reservoir in the Sichuan Basin.

2. Materials and Methods

2.1. Linearied PP-Wave Reflection Coefficient and Azimuthal EI including FFI

The construction of a fluid indicator is an essential step in the seismic characterization of reservoir fluid. Since natural vertical fractures are common in carbonate rocks, it is essential to consider fracture-induced anisotropy in the fluid identification of fractured carbonate reservoirs. Pan et al. [17] proposed the *FFI* for fluid identification in fractured reservoirs, which is expressed as:

$$FFI = g\frac{q\delta_N}{q\delta_T}, \tag{1}$$

with

$$q\delta_N = \frac{1}{1-\delta_{N0}}(\delta_N + 1 - \delta_{N0}),\ \ q\delta_T = \frac{1}{1-\delta_{T0}}(\delta_T + 1 - \delta_{T0}), \tag{2}$$

where $g = (V_S/V_P)^2$ is the squared S- to P-wave velocity ratio; δ_N and δ_T are the normal and tangential fracture weaknesses, respectively, δ_N is sensitive to the fluid in the reservoir, while δ_T is mainly related to the fracture density and does not vary with the fluid [31]; and $q\delta_N$ and $q\delta_T$ are the quasi normal and tangential fracture weaknesses, respectively. Rock physics analysis shows that *FFI* increases with fracture density when fractures are partially saturated with gas and water or oil [17]. Therefore, *FFI* can be used to detect fractures and identify fluids in fractured reservoirs.

Pan et al. [17] derived an approximate PP-wave reflection coefficient, $R_{pp}(\theta,\phi)$, in an HTI medium, which can be expressed as the sum of the isotropic background part $R_{pp}^{iso}(\theta)$ and the anisotropic perturbation part $R_{pp}^{ani}(\theta,\phi)$, as follows:

$$R_{pp}(\theta,\phi) = R_{pp}^{iso}(\theta) + R_{pp}^{ani}(\theta,\phi), \tag{3}$$

with

$$\begin{aligned} R_{pp}^{iso}(\theta) = &\ \tfrac{1}{2}\sec^2\theta\frac{\Delta I_P}{\overline{I_P}} - 4g\sin^2\theta\frac{\Delta I_S}{\overline{I_S}} + (2g\sin^2\theta - \tfrac{1}{2}\tan^2\theta)\frac{\Delta\rho}{\overline{\rho}}, \\ R_{pp}^{ani}(\theta) = &\ -g\left[\begin{array}{c}(\cos^2\phi\sin^2\theta + \sin^2\phi\cos^2\phi\sin^2\theta\tan^2\theta)(1-2g)\\ +\cos^4\phi\sin^2\theta\tan^2\theta(1-g)\end{array}\right]\Delta\delta_N \\ &+g\cos^2\phi\sin^2\theta(1-\sin^2\phi\tan^2\theta)\Delta\delta_T, \end{aligned} \tag{4}$$

where I_P, I_S, and ρ represent P-wave impedance, S-wave impedance, and density, respectively; Δ represents the difference in values between the interfaces; $\overline{\ }$ represents the mean values between the interfaces; θ is the incident angle; and $\phi = \phi_{obs} - \phi_{sym}$ is the azimuthal difference angle between the observed azimuth angle, ϕ_{obs}, and the azimuth of fracture normal, ϕ_{sym}.

Since the density term and the terms related to $\sin^2\theta\tan^2\theta$ only contribute to the reflection coefficient at large incident angles, under the assumption of weak anisotropy and a small incidence angle, we neglect these terms to yield

$$\begin{aligned} R_{pp}(\theta,\phi) = &\ \tfrac{1}{2}\sec^2\theta\frac{\Delta I_P}{\overline{I_P}} - 4g\sin^2\theta\frac{\Delta I_S}{\overline{I_S}} \\ &-g(1-2g)\cos^2\phi\sin^2\theta\Delta\delta_N + g\cos^2\phi\sin^2\theta\Delta\delta_T. \end{aligned} \tag{5}$$

The relationships between fracture weaknesses and quasi-fracture weaknesses are given by,

$$\Delta\delta_N = \frac{1}{2}\frac{\Delta q\delta_N}{\overline{q\delta_N}},\ \ \Delta\delta_T = \frac{1}{2}\frac{\Delta q\delta_T}{\overline{q\delta_T}}. \tag{6}$$

Substituting Equation (6) into Equation (5) and going through a series of derivations, we obtain a new PP-wave reflection coefficient in terms of P-wave impedance, P- to S-wave impedance ratio, *FFI*, and quasi-normal fracture weakness as follows:

$$\begin{aligned} R_{pp}(\theta,\phi) = & \left(\frac{1}{2}\sec^2\theta - 4g\sin^2\theta\right)\frac{\Delta I_P}{\overline{I_P}} + 4g\sin^2\theta\frac{\Delta(I_P/I_S)}{\overline{I_P/I_S}} \\ & -\frac{1}{2}\cos^2\phi\sin^2\theta\frac{\Delta FFI}{\overline{FFI}} + g^2\cos^2\phi\sin^2\theta\frac{\Delta q\delta_N}{\overline{q\delta_N}}. \end{aligned} \tag{7}$$

We use a two-layer model to analyze the accuracy of the new PP-wave reflection coefficient in Equation (7). The upper layer is an isotropic medium and the lower layer is an HTI medium. The elastic parameters and Thomsen anisotropy parameters of the model are given in Table 1.

Table 1. Model parameters.

Medium	$\mathbf{V_P(m/s)}$	$\mathbf{V_s(m/s)}$	$\boldsymbol{\rho}\mathbf{(kg/m)}$	$\boldsymbol{\varepsilon}^{(\mathbf{V})}$	$\boldsymbol{\delta}^{(\mathbf{V})}$	$\boldsymbol{\gamma}$
Isotropic overburden	4762	2724	2799	0	0	0
HTI medium	4542	2566	2667	−0.113	−0.275	0.167

Figure 1 shows the comparisons of the reflection coefficients calculated by the extended Zoeppritz's equation, Rüger's equation [14], and the new equation. Figure 1a,b show the reflection coefficient variation with the incident angle for azimuths of 0° and 90°, respectively. Figure 1c,d show reflection coefficient variation with azimuth for incident angles of 10° and 30°, respectively. We observe that the new approximation equation is basically consistent with the Rüger equation when the angle of incidence is less than 30°. Therefore, the newly derived approximate equation has acceptable accuracy and can be used to estimate *FFI*.

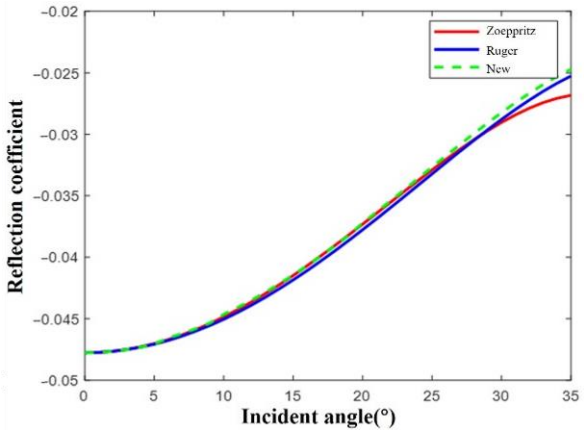

(**a**)

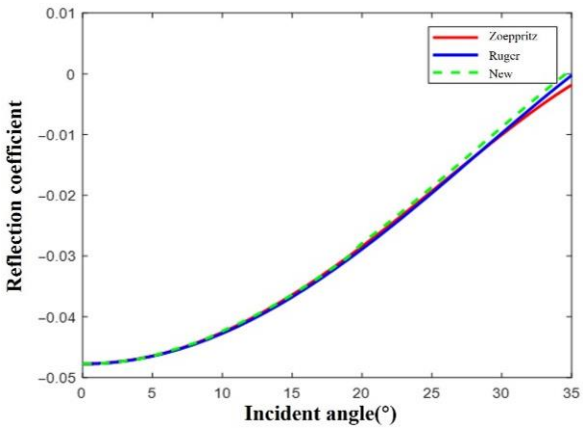

(**b**)

Figure 1. *Cont.*

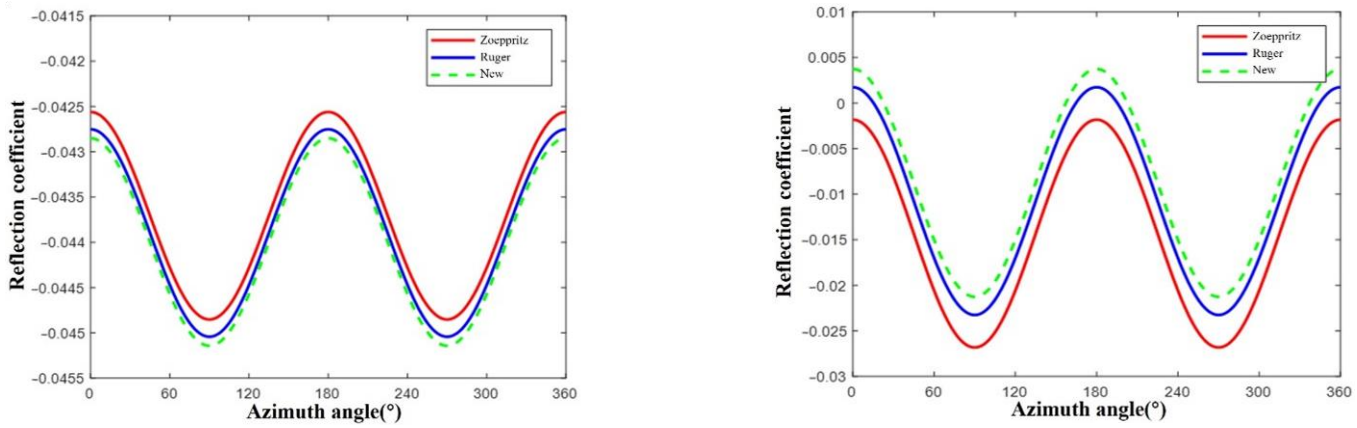

Figure 1. The comparison of the reflection coefficients calculated by the extended Zoeppritz's equation, Rüger's equation [14], and the derived new equation. (**a**) reflection coefficient variation with the incident angle for $\phi = 0°$; (**b**) reflection coefficient variation with the incident angle for $\phi = 90°$; (**c**) the reflection coefficient variation with azimuth for $\theta = 10°$; (**d**) reflection coefficient variation with azimuth for $\theta = 30°$.

According to the definition of EI, proposed by Connolly [29] and Martins [30], the reflection coefficient in HTI media can be written in terms of azimuthal EI as:

$$R_{pp}(\theta,\phi) \approx \frac{1}{2}\frac{\Delta EI(\theta,\phi)}{\overline{EI}} \approx \frac{1}{2} d \ln\left[\frac{EI(\theta,\phi)}{\overline{EI}}\right]. \tag{8}$$

Combining Equation (7) into Equation (8), we derive a new azimuthal EI equation as follows:

$$EI = \overline{EI}\left(\frac{I_P}{\overline{I_P}}\right)^{a(\theta)}\left(\frac{I_P/I_S}{\overline{I_P/I_S}}\right)^{b(\theta)}\left(\frac{FFI}{\overline{FFI}}\right)^{c(\theta,\phi)}\left(\frac{q\delta_N}{\overline{q\delta_N}}\right)^{d(\theta,\phi)} \tag{9}$$

where $\overline{EI} = \overline{I_P}$, $a(\theta) = \sec^2\theta - 8g\sin^2\theta$, $b(\theta) = 8g\sin^2\theta$, $c(\theta,\phi) = -2\cos^2\phi\sin^2\theta$, $d(\theta,\phi) = 4g^2\cos^2\phi\sin^2\theta$.

2.2. Bayesian EIVAZ Inversion for Direct Estimate of FFI

Taking the logarithm of both sides of the equation yields

$$\ln\left(\frac{EI}{\overline{EI}}\right) = a(\theta)\ln\left(\frac{I_P}{\overline{I_P}}\right) + b(\theta)\ln\left(\frac{I_P/I_S}{\overline{I_P/I_S}}\right) + c(\theta,\phi)\ln\left(\frac{FFI}{\overline{FFI}}\right) + d(\theta,\phi)\ln\left(\frac{q\delta_N}{\overline{q\delta_N}}\right). \tag{10}$$

For the case of M azimuths, N incident angles and K time samples, Equation (10) can be rewritten as a matrix of the form:

$$\mathbf{d}_{MNK\times 1} = \mathbf{G}_{MNK\times 4K}\mathbf{m}_{4K\times 1}, \tag{11}$$

where $\mathbf{d}$ represents the matrix of the normalized log-azimuthal EI, $\mathbf{G}$ represents the kernel function matrix composed of weighting coefficients for model parameters, and $\mathbf{m}$ represents the model parameter matrix to be inverted.

We implement the EIVAZ inversion approach to estimate the model parameters in a Bayesian framework [32,33]. In general, the noises are assumed to be independent and Gaussian. If we assume that the prior information for model parameters can be modeled using a Gaussian distribution, the posterior distribution for $\mathbf{m}$ given $\mathbf{d}$ is also Gaussian. The maximum a posteriori (MAP) solution for model parameters is given by Buland and Omre [34]:

$$\mathbf{m} = \mathbf{m}_0 + \mathbf{C_m}\mathbf{G}^{\mathrm{T}}\left(\mathbf{G}\mathbf{C_m}\mathbf{G}^{\mathrm{T}} + \mathbf{C_d}\right)^{-1}(\mathbf{d} - \mathbf{G}\mathbf{m}_0), \tag{12}$$

where $\mathbf{m}_0$ is the prior information of model parameters; $\mathbf{C_m}$ and $\mathbf{C_d}$ are covariance matrices of model parameters and noise, respectively; and the superscript T represents the transpose of a matrix.

To estimate *FFI* from observed azimuthal seismic data, we establish a two-step inversion workflow including (**1**) sparse pulse inversion for azimuthal EI volumes using observed azimuthal seismic data; and (**2**) estimation for the model parameter through the Bayesian EIVAZ inversion method.

3. Examples

3.1. Synthetic Example

A well log model and a 35 Hz Ricker wavelet are used to generate four azimuthal gathers (30°, 60°, 90°, and 120°). Synthetic seismic data are generated using Equation (7) based on the convolution model. Figure 2a shows that the four azimuthal angle gathers without noise. We added random noise to the synthetic seismic gathers. Figure 2b shows the generated seismic gathers with a signal-to-noise ratio (SNR) of two. We first stack the azimuthal angle gathers to generate three average incident angles (10°, 20°, and 30°) for each azimuth. Next, we perform sparse pulse inversion to estimate azimuthal EI. The inverted azimuthal EI is shown in Figure 3. The inversion results of azimuthal EI show an agreement with the true model. We then estimate model parameters from azimuthal EI to Bayesian EIVAZ inversion. The comparisons of the initial models (in green), true models (in blue), and inverted results (in red) of P-wave impedance, P- to S-wave impedance ratio, *FFI*, and quasi-normal fracture weakness for synthetic data without noise are shown, respectively, in Figure 4. We can see that the inversion results of P-wave impedance, P- to S-wave impedance ratio, *FFI*, and quasi-normal fracture weakness match well with the true model, thus proving the feasibility of our inversion method. Figure 5 shows the inversion results of azimuthal EI using this synthetic data, with SNR being two. We observe that the estimated azimuthal EI data also show acceptable accuracy. The inversion results of model parameters for synthetic data in the case of the SNR being two are displayed in Figure 6. From Figure 6, we also find that P-wave impedance, P- to S-wave impedance ratio, *FFI*, and quasi-normal fracture weakness are also estimated reasonably, which further confirms the stability and robustness of the inversion approach.

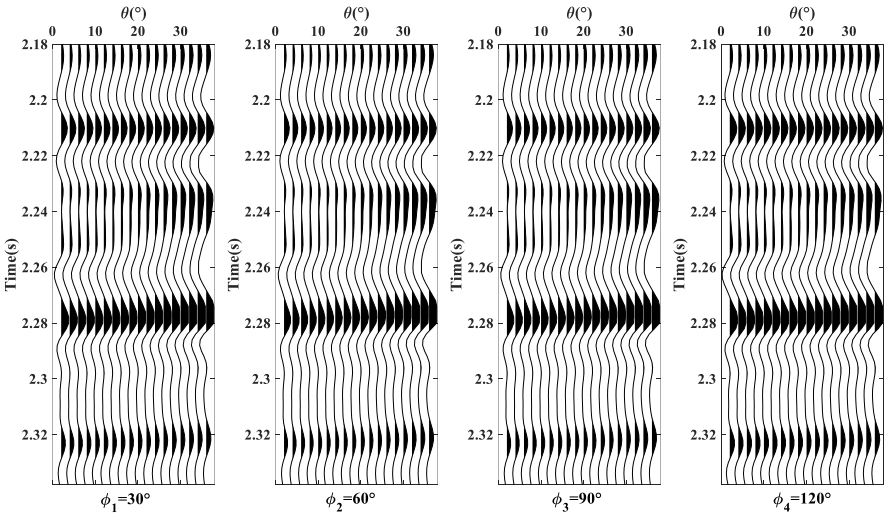

(**a**)

Figure 2. *Cont.*

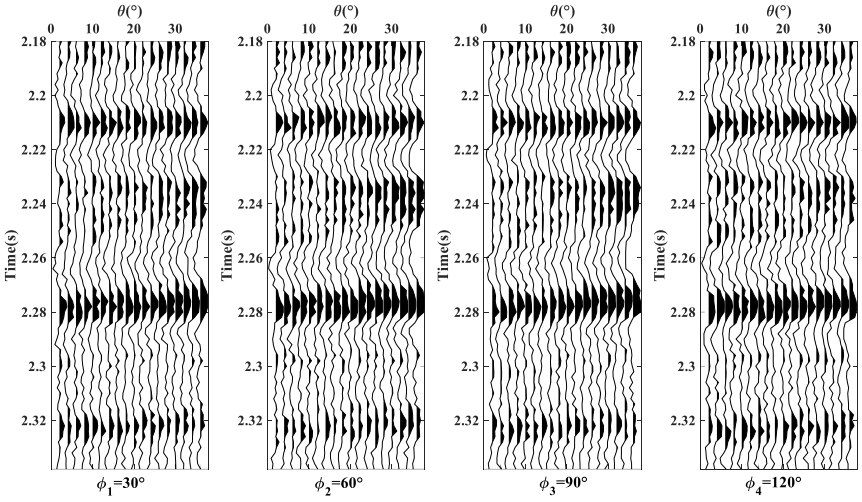

(**b**)

Figure 2. Synthetic azimuthal angle gathers with different levels of noise, where (**a**) shows the case without noise and (**b**) shows the case of SNR = 2.

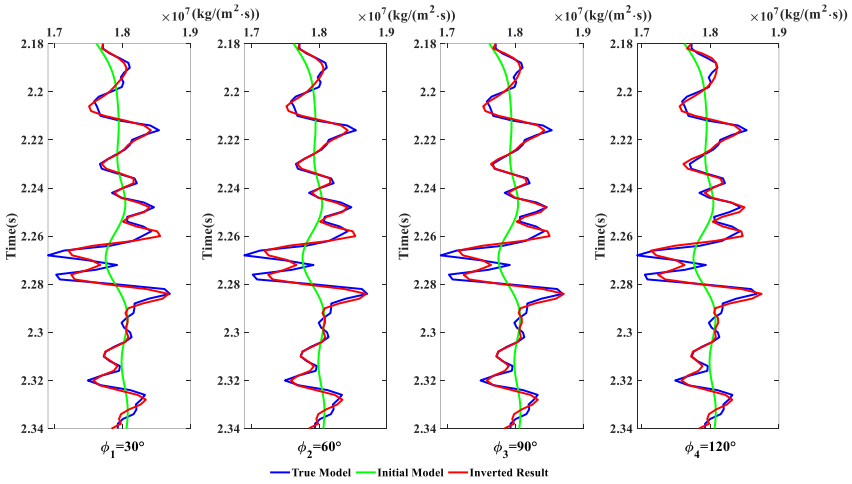

(**a**)

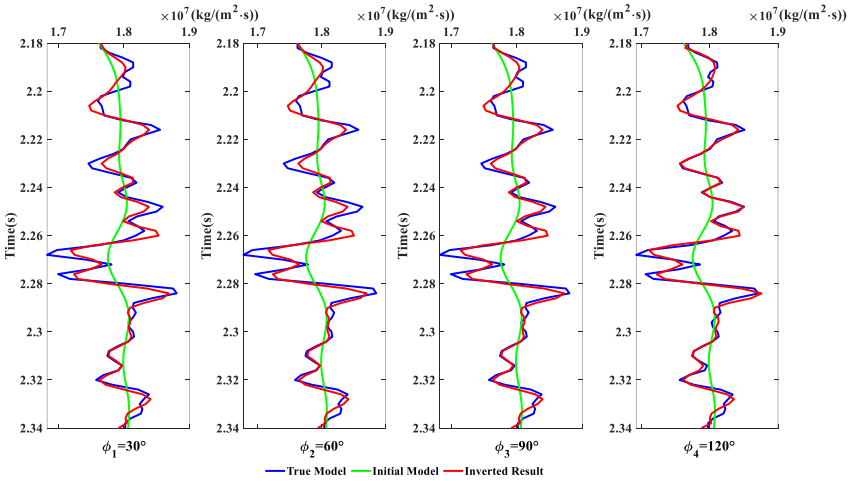

(**b**)

Figure 3. *Cont.*

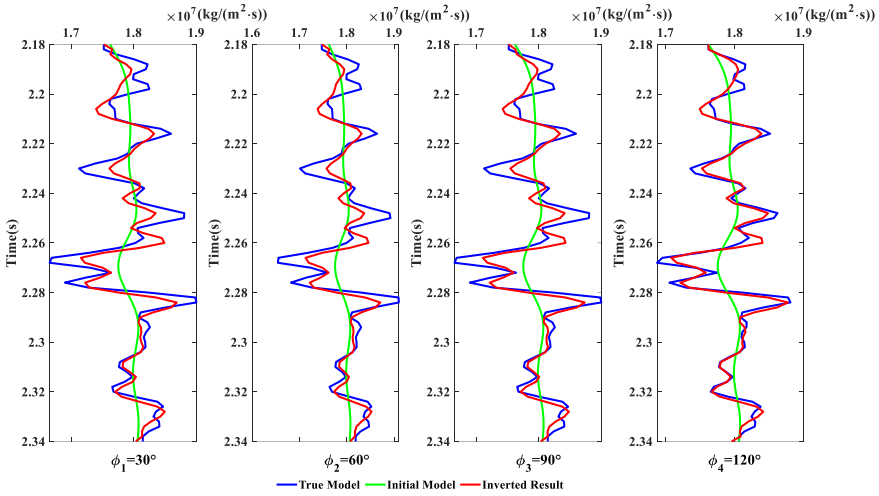

(**c**)

Figure 3. The estimated azimuthal EI of three angles and four azimuths without noise, where (**a**) $\theta = 10°$, (**b**) $\theta = 20°$, (**c**) $\theta = 30°$.

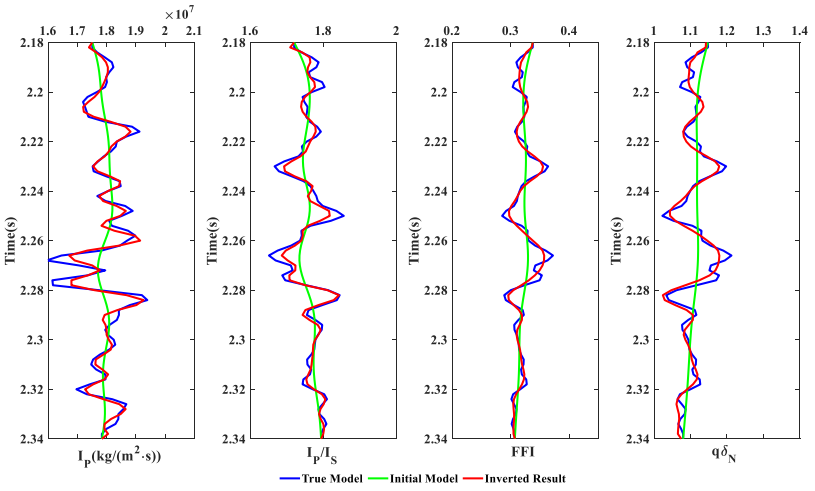

Figure 4. The inverted results of model parameters without noise.

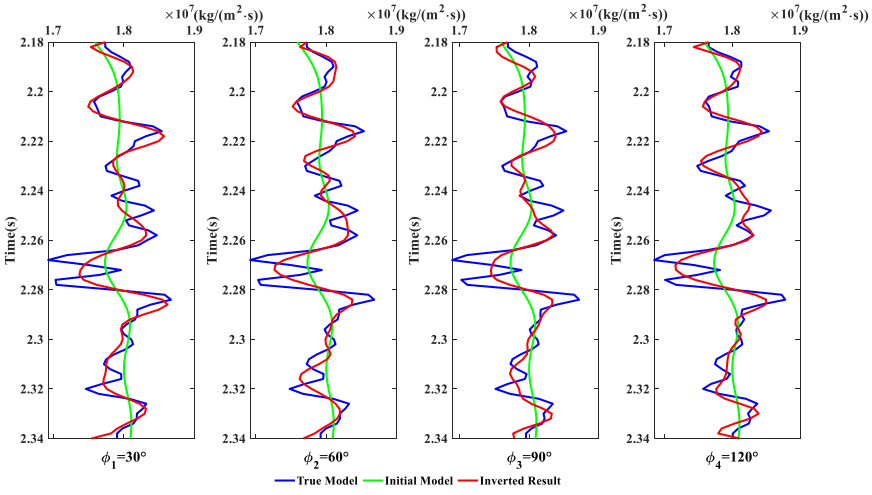

(**a**)

Figure 5. *Cont.*

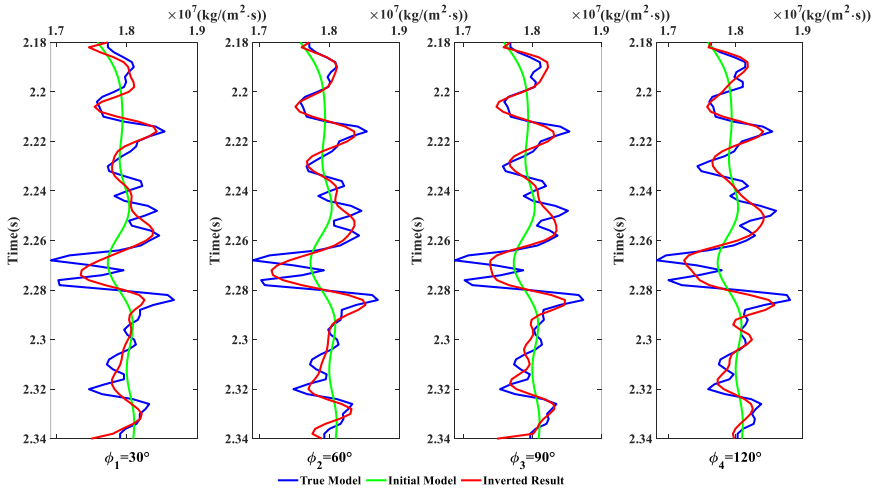

(**b**)

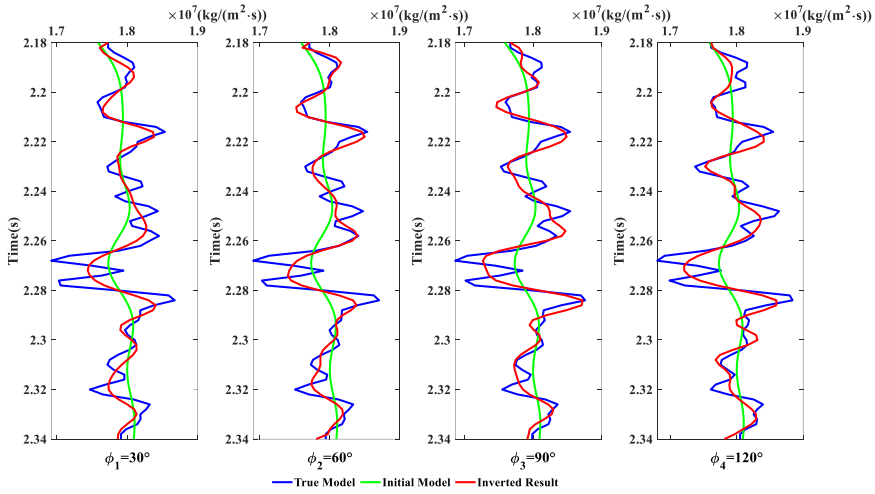

(**c**)

Figure 5. The estimated azimuthal EI with SNR = 2, where (**a**) $\theta = 10°$, (**b**) $\theta = 20°$, (**c**) $\theta = 30°$.

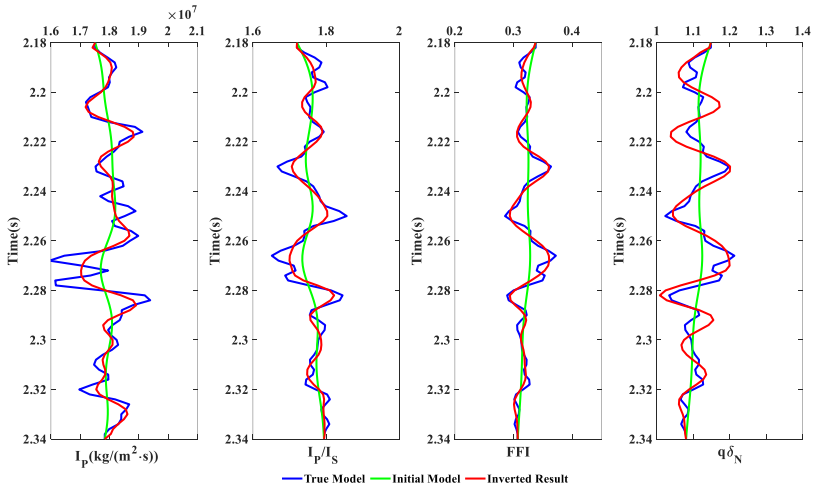

Figure 6. The inverted results of model parameters with SNR = 2.

3.2. Field Data Example

We apply the proposed approach to a real data set to confirm its feasibility further. The seismic data were acquired over a fractured carbonate-gas-bearing reservoir in southwest China. The tectonic location is located at the western end of the large uplift belt in the middle section of the West Sichuan Depression. The porosity of the target reservoir mainly distributes in the range of 2–4% with an average of 2.58%, and the permeability is generally lower than 0.1×10^{-3} μm^2. It is a tight reservoir with low-porosity and low-permeability, of which the thick gray dolomite is the main lithology. We first transfer the processed data from the offset domain to the incidence angle domain, and then sort and stack azimuthal angle gathers to generate azimuthal partial angle-stack seismic data, including four average azimuths and three average incident angles, shown in Figure 7. The four average azimuths are 27° (and a range of 8°–46°), 62° (and a range of 41°–83°), 98° (and a range of 78°–118°), and 134° (and a range of 113°–155°), and the three average incident angles for the near, mid, and far stacks are 9° (and a range of 2°–16°), 19° (and a range of 12°–26°), and 29° (and a range of 22°–36°). We observe that there is a strong negative reflection amplitude around the reservoir interface (at about 2.27 s). We then implement the sparse pulse inversion to estimate azimuthal EI by using the azimuthal partial angle-stack seismic data, and the inverted azimuthal EI profiles are shown in Figure 8. The inverted azimuthal EI shows relatively low values at the location of the reservoir. With the estimated azimuthal EI, we perform Bayesian EIVAZ inversion to estimate model parameters. Figure 9 shows the inverted model parameter profiles. We can see that around the reservoir, the inverted P-wave impedance and P- to S-wave impedance ratio show relatively low values, while the inverted *FFI* and quasi-normal fracture weakness show relatively high values, which indicates that the target reservoir is fractured and potentially gas-bearing. To verify the reliability of the inversion results, we plot the comparisons between the estimated model parameters and the corresponding well-logging values at the well location, as shown in Figure 10. The inverted results of P-wave impedance, P- to S-wave impedance ratio, *FFI*, and quasi-normal fracture weakness show an acceptable agreement with the well-logging data, which validates the feasibility of our method. Moreover, the inverted results of *FFI* and quasi-normal fracture weakness have good lateral continuity. These results help to guide fracture detection and hydrocarbon identification in fractured carbonate reservoirs.

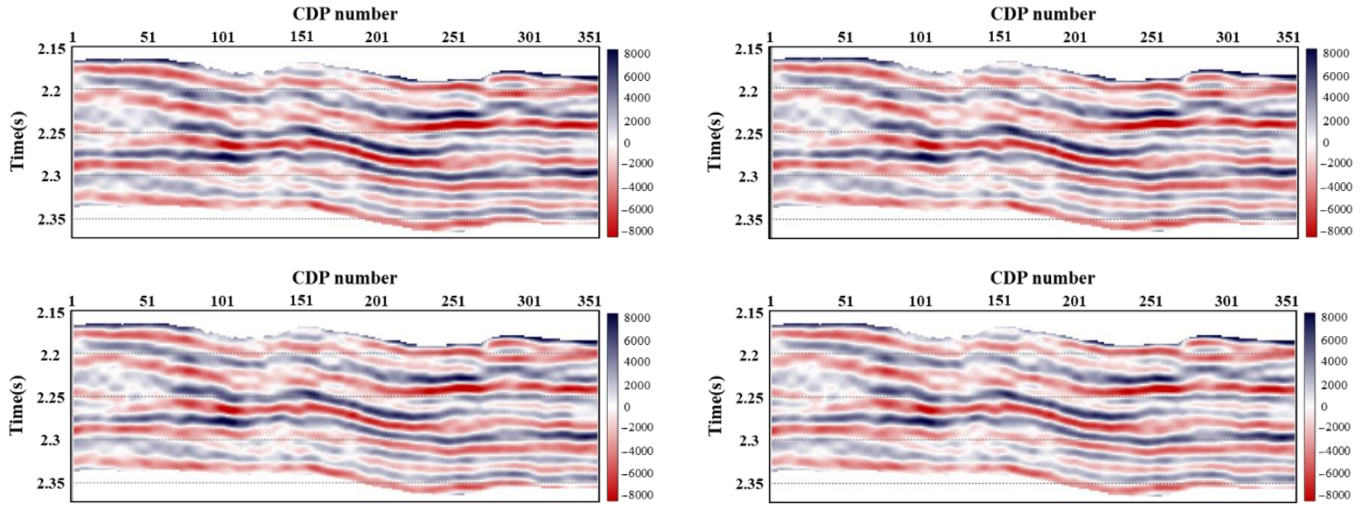

(**a**)

Figure 7. *Cont.*

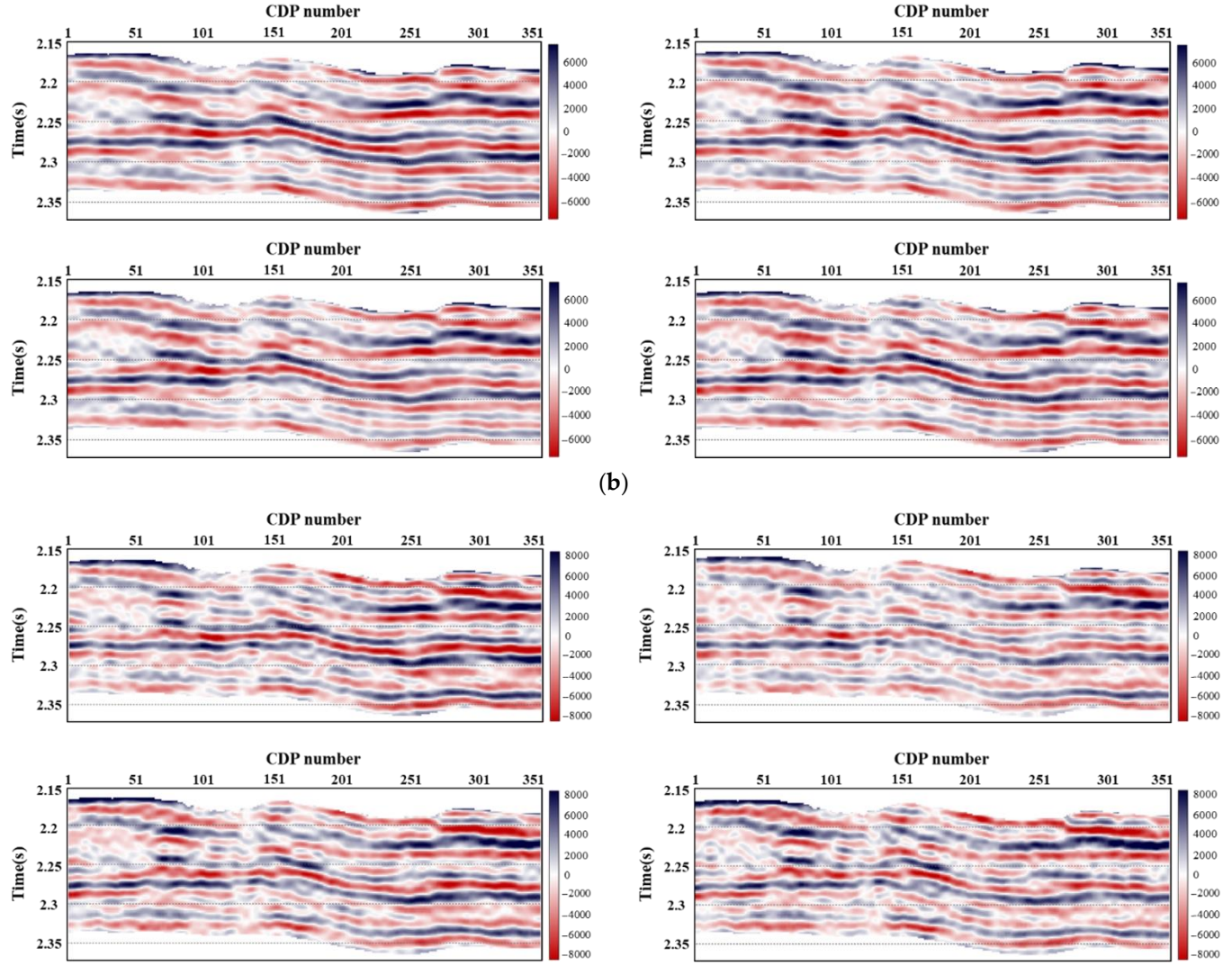

Figure 7. Different angles of seismic data for four azimuths: (**a**) small angle; (**b**) middle angle; (**c**) large angle.

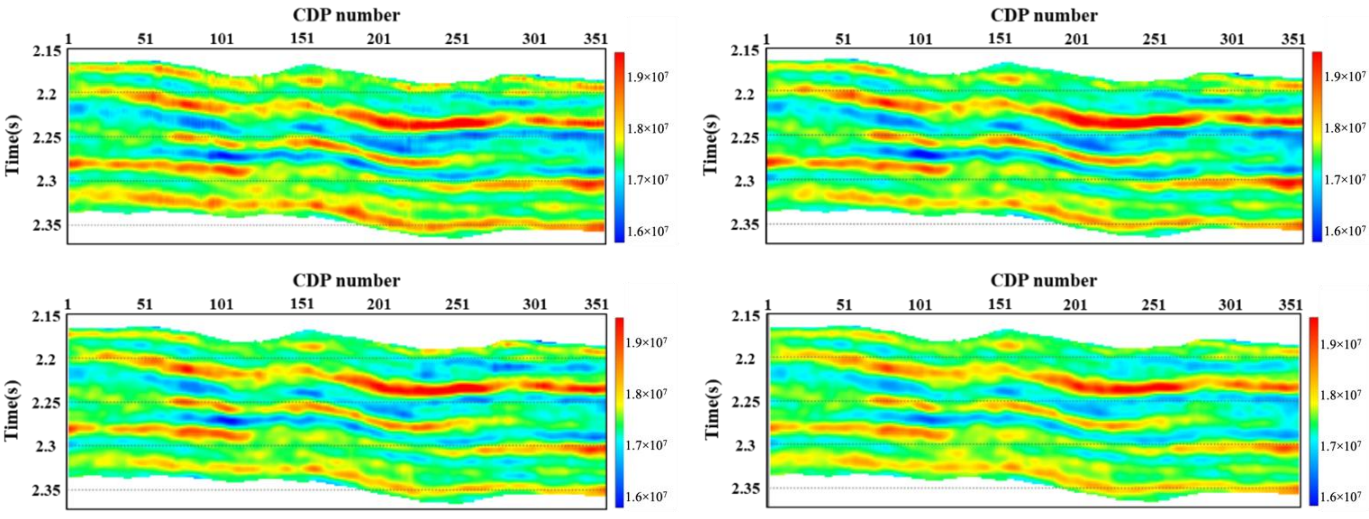

Figure 8. *Cont.*

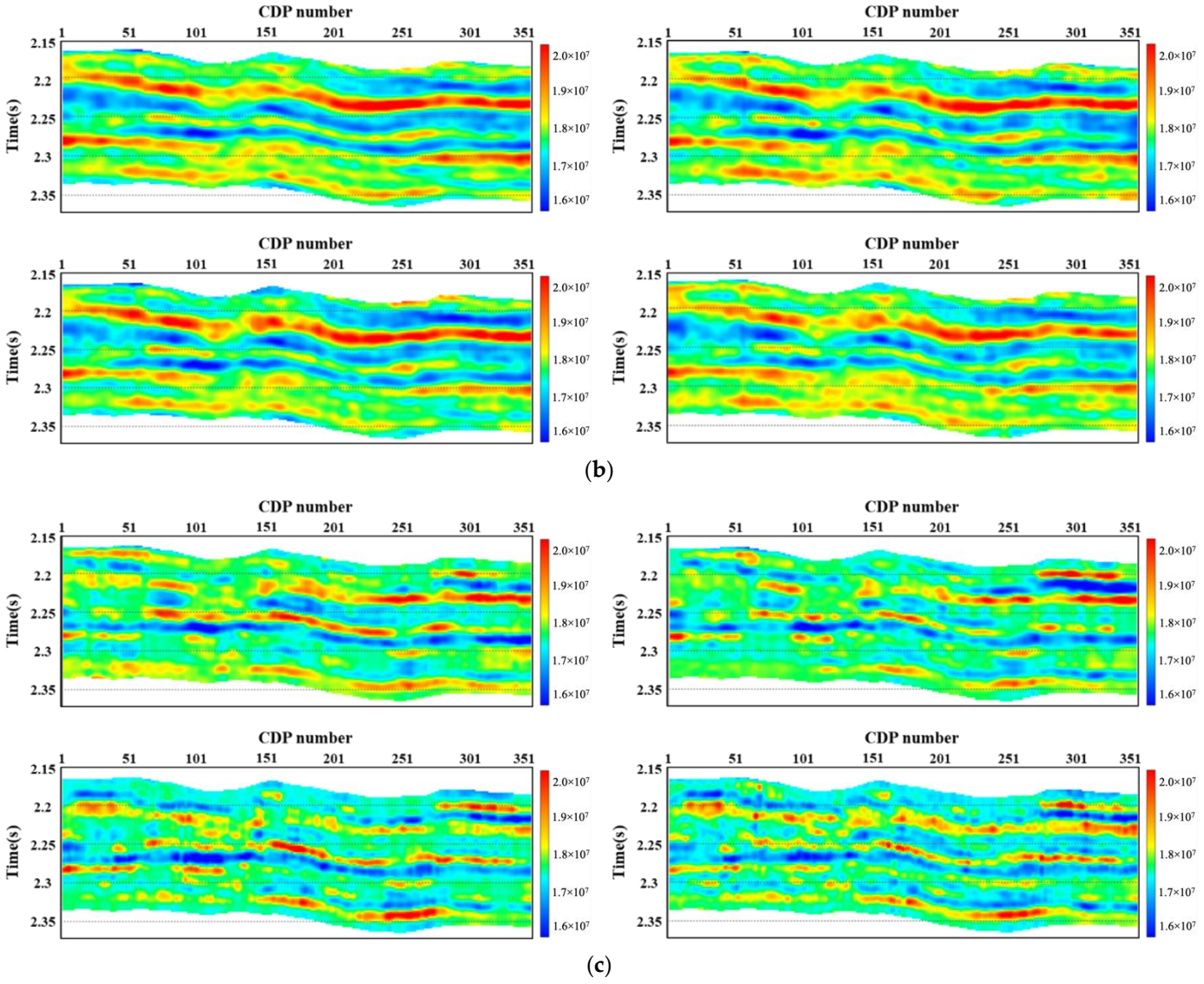

(**b**)

(**c**)

Figure 8. Estimated azimuthal EI datasets, where (**a**) small angle, (**b**) middle angle, and (**c**) large angle.

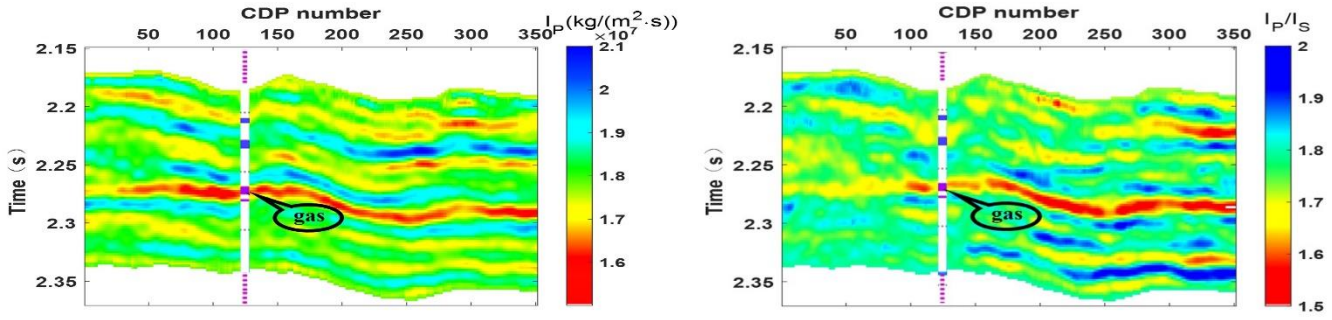

(**a**) (**b**)

Figure 9. *Cont.*

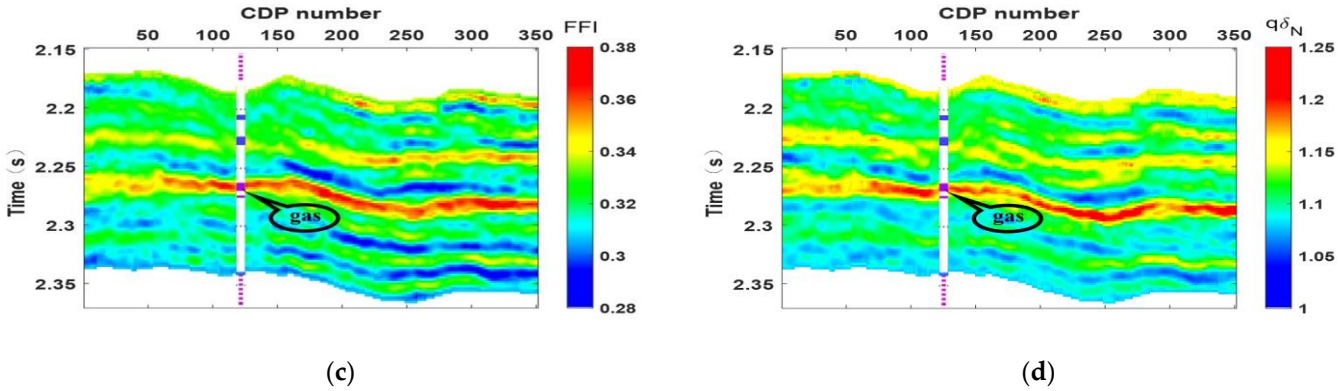

(**c**) (**d**)

Figure 9. Estimated model parameters from inverted azimuthal EI data: (**a**) P-wave impedance, (**b**) P- to S-wave impedance ratio, (**c**) *FFI*, and (**d**) quasi-normal fracture weakness.

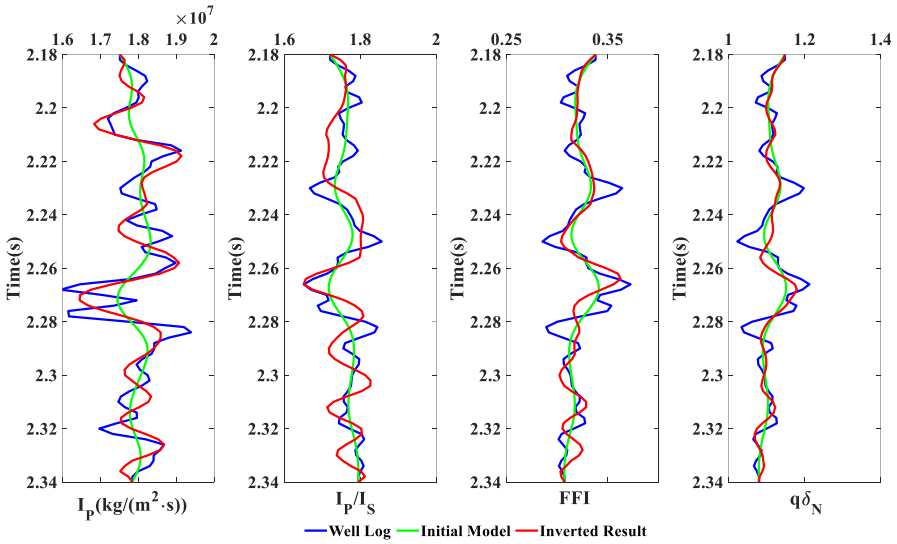

Figure 10. Comparison between the estimated model parameters and well logs at the well location.

4. Conclusions

Seismic fluid identification considering fracture-induced anisotropy is essential for the exploration and development of fractured carbonate reservoirs. We propose a novel Bayesian EIVAZ inversion approach for the direct estimate of a fracture fluid indicator, which could avoid cumulative errors in the indirect calculation process. Using the assumption of weak anisotropy and a small incident angle, we first derive a new approximate PP-wave coefficient as a function of P-wave impedance, P- to S-wave impedance ratio, *FFI*, and quasi-normal fracture weakness in an HTI medium. Analysis shows that the new approximation has acceptable accuracy at angles of incidence less than 30° and can be used to estimate the *FFI*. To estimate the *FFI* from observed azimuthal P-wave seismic reflection data, we deduce the azimuthal EI equation and establish a two-step inversion workflow involving (1) sparse pulse inversion for azimuthal EI volumes using observed azimuthal seismic data; and (2) model parameter estimates through the Bayesian EIVAZ inversion method. A synthetic data example demonstrates that the model parameters can be reasonably estimated even with moderate noise levels. The parameters obtained from the inversion are consistent with the true values. A field data example of a fractured carbonate-gas-bearing reservoir in the Sichuan Basin shows that our method can produce reliable inversion results of *FFI* and quasi-normal fracture weakness. We can see that around the reservoir, the inverted P-wave impedance and P- to S-wave impedance ratio show relatively low values, while the inverted *FFI* and quasi-normal fracture weakness show relatively high values, which indicates that the target reservoir is fractured and potentially gas-bearing. In addition, the inversion results of P-wave impedance, P- to S-wave

impedance ratio, *FFI*, and quasi-normal fracture weakness show acceptable agreement with the well logs, which indicates that our method can produce reasonable inversion results of P-wave impedance, P- to S-wave impedance ratio, *FFI*, and quasi-normal fracture weakness. The predicted results illustrate that the approach is feasible and robust and agrees well with the log data and geological interpretation. Compared with the conventional method, our approach has the greater advantage of accurately predicting the fracture fluid indicator. Moreover, the estimated profiles of *FFI* and quasi-normal fracture weakness have good lateral continuity; these results could help in the fracture detection and hydrocarbon identification of fractured carbonate reservoirs.

Besides, several ideal assumptions we have made in this study should be clearly stated. First, the inversion procedure presented in this paper is available when the effective fractures are a single suite of parallel vertical fractures embedded in an isotropic medium. However, when the complex gas-bearing carbonate reservoir develops two orthogonal vertical or a suite of tilted fractures embedded in a VTI or isotropic medium, the situation will be different. Secondly, the fluid identification methods of carbonate reservoirs with different pore systems are different and cannot be generalized. This paper focuses on the fluid identification method for deeply fractured carbonate reservoirs. Therefore, these assumptions restrict the applicability of the proposed inversion method, and we need to consider more complicated situations in the future.

Author Contributions: Conceptualization, X.G. and B.Y.; methodology, X.G.; software, J.Z.; validation, X.G., G.Z. and L.L; formal analysis, L.L., Y.Z. and R.Y.; writing—original draft preparation, X.G.; writing—review and editing, X.G., B.Y., G.Z. and L.L.; supervision, J.Z. All authors have read and agreed to the published version of the manuscript.

Funding: This research was funded by the Major science and technology projects of Exploration and production branch, Petrochina, Study on main controlling factors of high production and beneficial development technology policy of deep shale gas in western Chongqing (2022KT1205), the National Natural Science Foundation of China (U19B2008, U19B6003, 42074136, 41674130), the National Oil and Gas Major Projects of China (2016ZX05027004-001), the PetroChina Prospective, Basic, and Strategic Technology Research Project (2021DJ0606), and the Key technology and engineering test of shale gas benefit development in Guizhou Province (Guizhou Province Strategic Mineral Prospecting Technology Plan Project Contract [2022]ZD005).

Institutional Review Board Statement: Not applicable.

Informed Consent Statement: Not applicable.

Data Availability Statement: Data associated with this research are confidential and cannot be released.

Acknowledgments: Jason was provided by GeoSoftware by its university donation program.

Conflicts of Interest: The authors declare no conflict of interest.

References

1. Ostrander, W.J. Plane-wave reflection coefficients for gas sands at nonnormal angles of incidence. *Explor. Geophys.* **1984**, *15*, 193. [CrossRef]
2. Rutherford, S.R.; Williams, R.H. Amplitude-versus-offset variations in gas sands. *Geophysics* **1989**, *54*, 680–688. [CrossRef]
3. Castagna, J.P.; Swan, H.W.; Foster, D.J. Frame work for AVO gradient and intercept interpretation. *Geophysics* **1998**, *63*, 948–956. [CrossRef]
4. Chen, F.B.; Zong, Z.Y.; Jiang, M. Seismic reflectivity and transmissivity parameterization with the effect of normal in-situ stress. *Geophys. J. Int.* **2021**, *226*, 1599–1614. [CrossRef]
5. Smith, G.C.; Gidlow, P.M. Weighted stacking for rock property estimation and detection of gas. *Geophys. Prospect.* **1987**, *35*, 993–1014. [CrossRef]
6. Goodway, B.; Chen, T.; Downton, J. Improved AVO fluid detection and lithology discrimination using Lamé petrophysical parameters; "λρ","μρ", & "λ/μ fluid stack", from P and S inversions. In *SEG Technical Program Expanded Abstracts*; Society of Exploration Geophysicists: Tulsa, OK, USA, 1997; pp. 183–186. [CrossRef]
7. Gray, D. Elastic inversion for Lame parameters. In *SEG Technical Program Expanded Abstracts, Proceedings of the SEG 72th Annual Meeting, Salt Lake City, UT, USA, 6–11 October 2002*; Society of Exploration Geophysicists: Tulsa, OK, USA, 2002; pp. 213–216. [CrossRef]

8. Russell, B.H.; Hedlin, K.; Hilterman, F.J.; Lines, L.R. Fluid-property discrimination with AVO: A Biot-Gassmann perspective. *Geophysics* **2003**, *68*, 29–39. [CrossRef]
9. Russell, B.H.; Gray, D.; Hampson, D.P. Linearized AVO and poroelasticity. *Geophysics* **2011**, *76*, C19–C29. [CrossRef]
10. Zhang, S.X. Methodology and Application of Fluid Identification with Seismic Information. Ph.D. Thesis, China University of Petroleum (East China), Qingdao, China, 2012.
11. Yin, X.Y.; Zhang, S.X. Bayesian inversion for effective pore-fluid bulk modulus based on fluid-matrix decoupled amplitude variation with offset approximation. *Geophysics* **2014**, *79*, R221–R232. [CrossRef]
12. Chen, F.B.; Zong, Z.Y.; Yin, X.Y. Acoustothermoelasticity for joint effects of stress and thermal fields on wave dispersion and attenuation. *J. Geophys. Res. Solid Earth* **2022**, *127*, e2021JB023671. [CrossRef]
13. Zhang, J.L. Research and Application of Reservoir and Fluid Prediction Technique in Carbonate. Ph.D. Thesis, China University of Geosciences (Beijing), Beijing, China, 2014.
14. Rüger, A. P-wave reflection coefficients for transversely isotropic models with vertical and horizontal axis of symmetry. *Geophysics* **1997**, *62*, 713–722. [CrossRef]
15. Schoenberg, M.; Sayers, C.M. Seismic anisotropy of fractured rock. *Geophysics* **1995**, *60*, 204–211. [CrossRef]
16. Pan, X.P.; Zhang, G.Z. Fracture detection and fluid identification based on anisotropic Gassmann equation and linear-slip model. *Geophysics* **2019**, *84*, R85–R98. [CrossRef]
17. Pan, X.P.; Zhang, G.Z.; Yin, X.Y. Azimuthally anisotropic elastic impedance inversion for fluid indicator driven by rock physics. *Geophysics* **2017**, *82*, C211–C227. [CrossRef]
18. Chen, H.Z.; Ji, Y.X.; Innanen, K.A. Estimation of modified fluid indicator and dry fracture weaknesses using azimuthal elastic impedance. *Geophysics* **2018**, *83*, WA73–WA88. [CrossRef]
19. Golsanami, N.; Jayasuriya, M.N.; Yan, W.C.; Fernando, S.G.; Liu, X.; Cui, L.; Zhang, X.; Yasin, Q.; Dong, H.; Dong, X. Characterizing clay textures and their impact on the reservoir using deep learning and Lattice-Boltzmann simulation applied to SEM images. *Energy* **2022**, *240*, 122599. [CrossRef]
20. Li, L.; Zhang, G.Z.; Liu, J.Z.; Han, L.; Zhang, J.J. Estimation of fracture density and orientation from azimuthal elastic impedance difference through singular value decomposition. *Pet. Sci.* **2021**, *18*, 1675–1688. [CrossRef]
21. Li, L.; Zhang, G.Z.; Pan, X.P.; Liu, J.X. Estimating Effective Stress Parameter and Fracture Parameters in Shale-Gas Fractured Reservoirs Using Azimuthal Fourier Coefficients. *Surv. Geophys.* **2021**, *42*, 1377–1400. [CrossRef]
22. Pan, X.P.; Zhao, Z.Z.; Zhou, S.X.; Zhao, X.L.; Xu, K.; Ge, Z.J.; Zhang, G.Z.; Liu, J.X. Detection of natural tilted fractures from azimuthal seismic amplitude data based on linear-slip theory. *IEEE Trans. Geosci. Remote Sens.* **2021**, *60*, 5907414. [CrossRef]
23. Pan, X.P.; Lu, C.X.; Zhang, G.Z.; Pu, W.; Liu, J.X. Seismic Characterization of Naturally Fractured Reservoirs with Monoclinic Symmetry Induced by Horizontal and Tilted Fractures from Amplitude Variation with Offset and Azimuth. *Surv. Geophys.* **2022**, *43*, 815–851. [CrossRef]
24. Chen, H.Z.; Zhang, G.Z. Estimation of dry fracture weakness, porosity, and fluid modulus using observable seismic reflection data in a gas-bearing reservoir. *Surv. Geophys.* **2017**, *38*, 651–678. [CrossRef]
25. Pan, X.P.; Zhang, G.Z. Estimation of fluid indicator and dry fracture compliances using azimuthal seismic reflection data in a gas-saturated fractured reservoir. *J. Pet. Sci. Eng.* **2018**, *167*, 737–751. [CrossRef]
26. Pan, X.P.; Zhang, G.Z.; Cui, Y. Matrix-fluid-fracture decoupled-based elastic impedance variation with angle and azimuth inversion for fluid modulus and fracture weaknesses. *J. Pet. Sci. Eng.* **2020**, *189*, 106974. [CrossRef]
27. Li, L.; Zhang, G.Z.; Pan, X.P.; Guo, X.L.; Zhang, J.J.; Zhou, Y.; Lin, Y. Anisotropic Poroelasticity and AVAZ Inversion for in Situ Stress Estimate in Fractured Shale-Gas Reservoirs. *IEEE Trans. Geosci. Remote Sens.* **2022**, *60*, 5911113. [CrossRef]
28. Thomsen, L. Weak elastic anisotropy. *Geophysics* **1986**, *51*, 1954–1966. [CrossRef]
29. Connolly, P. Elastic impedance. *Lead. Edge* **1999**, *18*, 438–452. [CrossRef]
30. Martins, J.L. Elastic impedance in weakly anisotropic media. *Geophysics* **2006**, *71*, D73–D83. [CrossRef]
31. Bakulin, A.; Grechka, V.; Tsvankin, I. Estimation of fracture parameters from reflection seismic data—Part I: HTI model due to a single fracture set. *Geophysics* **2000**, *65*, 1788–1802. [CrossRef]
32. Chen, F.B.; Zong, Z.Y.; Yang, Y.M.; Gu, X.Y. Amplitude-variation-with-offset inversion using P- to S-wave velocity ratio. *Geophysics* **2022**, *87*, N63–N74. [CrossRef]
33. Ulrych, T.J.; Sacchi, M.D.; Woodbury, A. A Bayes tour of inversion: A tutorial. *Geophysics* **2001**, *66*, 55–69. [CrossRef]
34. Buland, A.; Omre, H. Bayesian linearized AVO inversion. *Geophysics* **2003**, *68*, 185–198. [CrossRef]